Journal of Electrical Engineering & Technology (2026) 21:3757–3769
https://doi.org/10.1007/s42835-026-02651-w

ORIGINAL ARTICLE

Effective Load Identification for Inductive Wireless Power Transfer Systems Utilizing Kalman Filter Approach

Andrew Ngini Mwangi[1] · Sung-Jin Choi[1]

Received: 4 October 2025 / Revised: 26 January 2026 / Accepted: 28 January 2026 / Published online: 25 February 2026

Abstract

This article presents an effective load estimation strategy that pairs an analytical model with a dynamic Kalman estimator for Inductive Wireless Power Transfer (IWPT) system that eliminates feedback from the secondary-side to the primary-side. Given that sensed primary-side current and voltage quantities are vulnerable to noise, conventional approaches tend to propagate this noise, thereby impacting the accuracy and tracking of the identified load parameters. Therefore, this article proposes the implementation of a two-step strategy for identification under varying output load conditions. First, the output load resistance is estimated analytically as a baseline parameter. Then, based on the recognized resistance parameter, a state-space dynamic Kalman model of the system is derived to track the output load voltage. This two-step identification strategy has the advantage of robust estimation in the presence of noise and load variations as it decouples the nonlinear system via a linear estimator. The efficacy of the proposed identification approach is confirmed through simulation and experimental validation using a 75 W IWPT hardware test-bench. Under dynamic operation, the proposed two-step identification approach reduces the estimation error by 32% at maximum variation range.

Keywords Inductive wireless power transfer systems · Kalman filter · Parameter identification · State-space model

1 Introduction

Inductive Wireless Power Transfer (IWPT) technology has become a cornerstone for innovation in charging applications ranging from consumer electronics to transportation, offering convenience and enhanced safety [1–3]. A fundamental challenge in designing these systems is maintaining the power transfer efficiency, which is critically dependent on accurately identifying the system parameters, especially those located on the secondary-side of the system [4, 5]. However, in practically implemented IWPT systems that eliminate communication links in order to reduce cost and complexity, the secondary-side parameters are difficult to measure directly [6, 7]. Furthermore, the occurrence of load variations necessitates the implementation of sensors to detect this change by use of in-band or out-of-band sensing of the wireless system. In this case, load modulation is achieved via primary-side control techniques, hence the need for secondary-side parameter estimation. For instance, when the equivalent load resistance varies during charging process, output regulation will require the recognized output parameters.

To address this challenge, numerous parameter identification techniques have been developed, each with their distinct trade-offs [8]. The most traditional are analytical methods, which use the circuit model equations and primary-side measurements of the system to solve for unknown parameters like load resistance and output load voltage [9, 10]. While computationally simple, these methods are notoriously vulnerable to inevitable measurement noise and process noise [11]. The reliance on an idealized system model means that their accuracy will degrade significantly under non-ideal operating conditions. Next identification technique in literature is the signal-processing techniques [12, 13]. The work in [12] using Fast Fourier transforms handles noise by using multiple interharmonics but at a steep cost of

✉ Sung-Jin Choi
sjchoi@ulsan.ac.kr

Andrew Ngini Mwangi
nginiandrew79@gmail.com

[1] Department of Electrical, Electronic and Computer Engineering, University of Ulsan, Ulsan 44610, Republic of Korea

high computational complexity and a requirement for very high sampling rates to achieve targeted accuracy.

Another applied approach is to actively perturb the system to identify its parameters. In [14, 15], frequency-sweeping methods, for example, sweep the excitation frequency and observe the response to determine resonance peaks through which parameters can be derived. A major drawback of this identification technique is that it inherently disrupts normal power transfer during the sweep. Moreover, its accuracy can be compromised in noisy environments or when the sweep range is limited. A proposal in [16] is a method that is based on addition of auxiliary measurement circuit such as auxiliary sensing loop coil in the system which can yield robust estimates without interrupting power transfer, but this is done so at the cost of increased hardware complexity, size, and expense. A common ground for these diverse methods is a persistent dilemma of a choice between simple, low-cost methods that lack robustness, and more accurate methods that are complex, disruptive and/or expensive.

The inherent limitations of these conventional techniques, particularly their vulnerability to noise and inability to adapt to dynamic load changes without operational disruption, highlight the need for a robust, real-time estimation strategy. State-space observers, and specifically the Kalman filter [17, 18], provide a powerful framework for estimating states in dynamic systems corrupted by noise. The Kalman filter's recursive nature makes it exceptionally well-suited for tracking time-varying parameters in real time.

Conventional observer-based approaches, such as extended Kalman filter (EKF) [17], typically attempt to estimate states and unknown parameters simultaneously. These approaches require linearization of a nonlinear model which introduces linearization error, compounding additional computational error. On the other hand, the two-step framework proposed in this paper first obtains a baseline analytical estimate of the equivalent AC load resistance and then uses this estimate to form a time-varying but linear state transition matrix for the linear Kalman filter model. This decoupling structure avoids nonlinear estimation of the AC load resistance inside the filter, hence offering a favorable trade-off: first step to account for the nonlinearity while second step retains relative computational simplicity of the Kalman filter. Therefore, this paper proposes an effective identification strategy that leverages the strengths of both analytical and filter-based approaches of Kalman estimator to identify dynamic output parameters, considering that the coupling is defined as the transmitting and receiving platforms are under guided positioning in accordance with Qi wireless charging standards [19]. The contributions of this work are as follows:

1. A robust two-step identification framework that first uses an analytical model to obtain an initial estimate of the equivalent alternating current (ac) load resistance, R_{eq}, which is then crucially used to inform the state-space model for the Kalman estimator.
2. By dedicating the Kalman estimator to a single, well-defined task of tracking the output direct current (dc) voltage, this approach maintains tracking and robustly handles load changes and significant measurement noise.
3. The proposed strategy is a practical, non-disruptive implementation as it relies solely on acquisition of primary-side quantities, offering reliable online (real-time) load identification in IWPT systems.

The rest of this article is organized as follows. Section 2 outlines identification in IWPT system and noise impact of conventional identification. Section 3 derives the state-space Kalman estimator model. Section 4 presents simulation and experimental validation for this two-step identification method. Section 5 concludes the article.

2 Load Parameters Identification in IWPT System

Figure 1 demonstrates a general IWPT system with primary-side identification. The transmitter side is comprised of a dc source, high frequency (HF) inverter and input matching network (IMN), the coupler constitutes different geometrically designed coupling coils, and the receiver is made of output matching network (OMN), rectifier and load. Input primary-side voltage and current are obtained from the IMN on the transmitter side and are fed into the primary-side identification technique. The resulting estimated parameters are then utilized for load modulation that is implemented in the primary-side controller.

2.1 Configuration of SS-IWPT System

In numerous articles published in literature, a series-series (SS) compensated system is the most commonly used topology with the IWPT system. Following this, the analysis in this paper will also utilize the SS topology as illustrated in Fig. 2. On the primary side, a DC voltage source V_{DC} powers a full-bridge inverter (switches S_1–S_4) that generates a high-frequency ac voltage V_p. I_p is the current through the primary resonant tank, which consists of a compensation capacitor C_p in series with the primary coil self-inductance L_p and its equivalent series resistance R_p. M is the mutual inductance linking the primary-side and secondary-side self-inductances. The secondary resonant tank, comprising

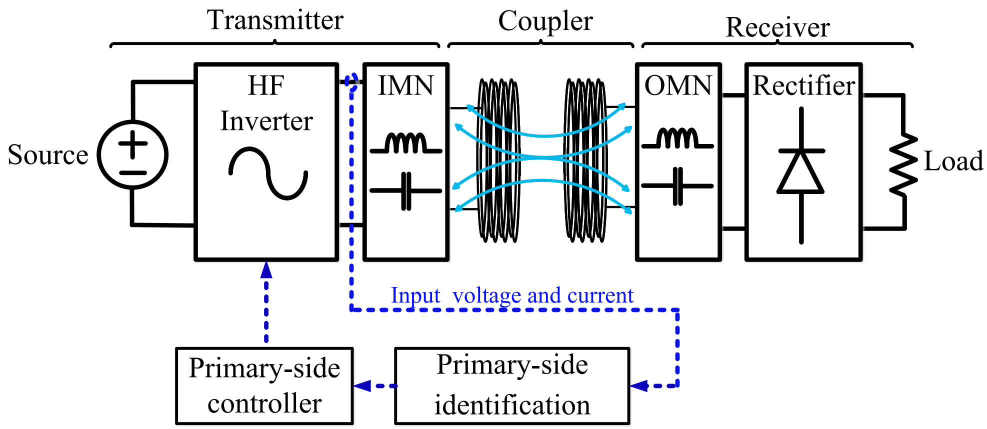

Fig. 1 Primary-side identification in IWPT system

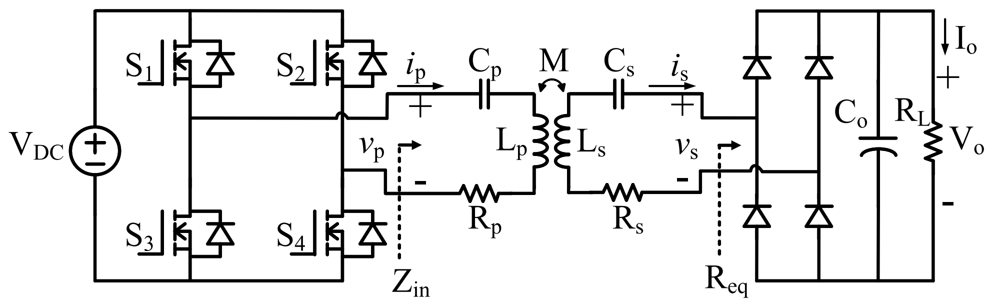

Fig. 2 Configuration of SS-IWPT system

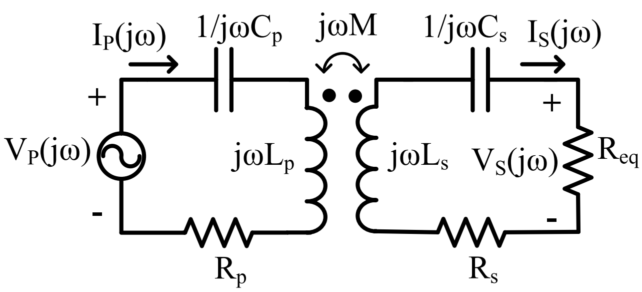

Fig. 3 Equivalent circuit of SS-compensated IWPT system

a series compensation capacitor C_s and the secondary coil self-inductance L_s with its equivalent series resistance R_s, resonates to maximize power transfer, resulting in a secondary ac voltage V_s and current I_s. This ac current is rectified by the full-wave rectifier, smoothed by an output filter capacitor C_o, and delivered to the output load resistor R_L, producing a final DC output voltage V_o and current I_o. Under the ideal diode assumption, the rectifier and load present an equivalent ac resistance R_{eq} to the secondary resonant circuit.

2.2 Noise Impact of Sole Analytical-Based Conventional Identification

Analytical-based conventional identification is based off of the system equivalent circuit model. The equivalent circuit schematic of the SS-compensated IWPT is shown in Fig. 3. Assuming fundamental harmonic approximation using Kirchhoff's voltage law analysis, the equivalent input impedance Z_{in} seen from the primary side is derived to be

$$Z_{in} = R_p + j\omega L_p + \frac{1}{j\omega C_p} + \frac{(\omega M)^2}{Z_s} \tag{1}$$

where Z_s is the secondary-side impedance given as

$$Z_s = R_s + j\omega L_s + \frac{1}{j\omega C_s} + R_{eq}. \tag{2}$$

From (1), the real and imaginary parts of the equivalent input impedance are given as

$$R_{in} = R_p + \frac{\omega^2 M^2 (R_s + R_{eq})}{(R_s + R_{eq})^2 + (\omega L_s - 1/\omega C_s)^2} \tag{3}$$

and

$$X_{in} = \omega L_p - \frac{1}{\omega C_p} - \frac{(\omega L_s - 1/\omega C_s)\,\omega^2 M^2}{(R_s + R_{eq})^2 + (\omega L_s - 1/\omega C_s)^2} \tag{4}$$

where (3) and (4) are simplified by equating same denominator terms on the right-hand side to obtain

$$\frac{\omega^2 M^2 (R_{eq} + R_s)}{R_{in} - R_p} = \frac{(\omega L_s - 1/\omega C_s)}{X_{in} - \omega L_p + 1/\omega C_p} \tag{5}$$

and thus, equivalent AC load resistance can be estimated as

$$R_{eq} = -\frac{(R_{in} - R_p)(\omega L_s - 1/\omega C_s)}{X_{in} - \omega L_p + 1/\omega C_p} - R_s. \tag{6}$$

This R_{eq} is transformed to the load resistance R_L by the power balance for the lossless full bridge rectifier as

$$R_L = \frac{8}{\pi^2}\left(-\frac{(R_{in} - R_p)(\omega L_s - 1/\omega C_s)}{X_{in} - \omega L_p + 1/\omega C_p} - R_s\right). \tag{7}$$

The rms of the fundamental component of the voltage across R_{eq} is given by

$$V_{s1,rms} = I_{s1,rms}\, R_{eq} \tag{8}$$

where $I_{s1,rms}$ is the rms of the fundamental component of the secondary-side current given by

$$I_{s1,rms} = \left|\frac{j\omega M I_{p1,rms}}{Z_s}\right|. \tag{9}$$

Hence, the full-wave bridge rectifier produces approximately the average value of the full-wave rectified output load voltage [10] as

$$V_o = \frac{2\sqrt{2}}{\pi}\left|\frac{j\omega M I_{p1,rms}}{R_s + j\omega L_s + 1/j\omega C_s + R_{eq}}\right| R_{eq}. \tag{10}$$

These estimations are executed with the aid of measured primary-side current and voltage to determine the R_{in} and X_{in} terms as

$$R_{in} = \frac{V_{p1,rms}}{I_{p1,rms}}\cos\theta \tag{11}$$

and

$$X_{in} = \frac{V_{p1,rms}}{I_{p1,rms}}\sin\theta \tag{12}$$

where $V_{p1,rms}$ and $I_{p1,rms}$ are the rms values of the fundamental components of the primary-side voltage and current, respectively, and θ is the phase difference between fundamental components of the primary-side voltage and current during operation.

To illustrate noise impact on the sole analytical identification process, the process begins with raw, noisy sensed quantities of the primary-side voltage and current. These noisy signals, $v_{\mathrm{p,sens}}(t)$ and $i_{\mathrm{p,sens}}(t)$, can be modeled as the sum of the true signal and additive white Gaussian noise (AWGN) terms n_v and n_i.

$$v_{\mathrm{p,sens}}(t) = v(t) + n_v(t), \quad \text{where } n_v(t) \sim \mathcal{N}(0, \sigma_v^2) \tag{13}$$

$$i_{\mathrm{p,sens}}(t) = i(t) + n_i(t), \quad \text{where } n_i(t) \sim \mathcal{N}(0, \sigma_i^2) \tag{14}$$

Here, the variances σ_v^2 and σ_i^2 quantify the noise introduced by the voltage and current sensors, respectively, with zero mean. These noisy, instantaneous signals are then processed to calculate their rms values. This step carries the noise from the time domain into the estimated parameters. The resulting noisy rms values can be approximated as the true rms value plus an equivalent noise amplitude, N_v and N_i

$$V_{\mathrm{p1,rms,sens}} \approx V_{\mathrm{p1,rms,true}} + N_v \tag{15}$$

$$I_{\mathrm{p1,rms,sens}} \approx I_{\mathrm{p1,rms,true}} + N_i \tag{16}$$

These noisy sensed values are the direct inputs for calculating the input impedance of the system using (11) and (12). Consequently, the calculated impedance parts, R'_{in} and X'_{in}, will also be erroneous, composed of their true values plus noise-induced error terms, δR_{in} and δX_{in}.

$$R'_{in} = \frac{V_{\mathrm{p1,rms,sens}}}{I_{\mathrm{p1,rms,sens}}}\cos\theta = R_{in} + \delta R_{in} \tag{17}$$

$$X'_{in} = \frac{V_{\mathrm{p1,rms,sens}}}{I_{\mathrm{p1,rms,sens}}}\sin\theta = X_{in} + \delta X_{in} \tag{18}$$

The propagation of these intermediate errors influences the estimation of the equivalent load resistance, R'_{eq}, modifying the formula in (6). To explore how, R_{eq} is linearized around R_{in}, X_{in} using a first-order Taylor expansion to give

$$\begin{aligned} R'_{eq} &= f(R'_{in}, X'_{in}) \\ &\approx f(R_{in}, X_{in}) + \left.\frac{\partial f}{\partial R_{in}}\right|_{(R_{in}, X_{in})} \delta R_{in} \\ &+ \left.\frac{\partial f}{\partial X_{in}}\right|_{(R_{in}, X_{in})} \delta X_{in}. \end{aligned} \tag{19}$$

Hence, the estimation error can be written as

$$\delta R_{eq} = R_{eq}\prime - R_{eq} \approx \frac{\partial R_{eq}}{\partial R_{in}}\delta R_{in} + \frac{\partial R_{eq}}{\partial X_{in}}\delta X_{in}. \tag{20}$$

Since δR_{in} and δX_{in} are assumed to be zero-mean and are uncorrelated, then the variance of δR_{eq} can be expressed as the weighted sum of the variances of δR_{in} and δX_{in}, which are given by the squared partial derivatives

$$\mathrm{Var}[R_{eq}\prime] \approx \left(\frac{\partial R_{eq}}{\partial R_{in}}\right)^2 \mathrm{Var}[\delta R_{in}] + \left(\frac{\partial R_{eq}}{\partial X_{in}}\right)^2 \mathrm{Var}[\delta X_{in}]. \tag{21}$$

Noting that the output voltage V_o in (10) depends on R_{eq}, any uncertainty in R_{eq} will be propagated into V_o. Denoting

Table 1 Circuit parameters for simulation and experiment

Symbol	Parameters	Value
L_p	Primary coil self-inductance	155.40 μH
L_s	Secondary coil self-inductance	156.56 μH
M	Mutual inductance	41.54 μH
C_p	Primary-side compensation capacitance	15.88 nF
C_s	Secondary-side compensation capacitance	16.30 nF
R_p	Primary coil equivalent series resistance	0.1434 Ω
R_s	Secondary coil equivalent series resistance	0.1474 Ω

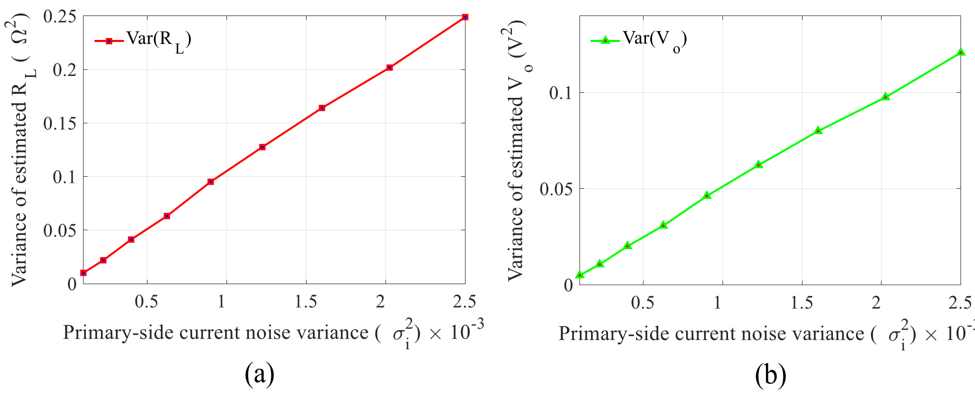

Fig. 4 Effect of sensed noise variance on the variance of estimated R_L and V_o

this dependence as $V_o \propto g(R_{eq})$ where g represents the other quantities in the equation, and linearizing gives

$$V_o\prime \approx V_o + \frac{\partial V_o}{\partial R_{eq}}\,\delta R_{eq}. \tag{22}$$

Therefore, the variance of the estimated output voltage is

$$\mathrm{Var}[V\prime_o] \approx \left(\frac{\partial V_o}{\partial R_{eq}}\right)^2 \mathrm{Var}[R\prime_{eq}] \tag{23}$$

The expression in (21) shows that the initial measurement variances, which originate from σ_v^2 and σ_i^2, are amplified by the square of the factors inherent in the identification formula. This explains that the sole analytical approach is structurally prone to noise as it is propagated in subsequent operations. The error in the estimated load resistance is cascaded to the final output voltage estimation. The resulting variance of the estimated output voltage, $\mathrm{Var}[V\prime_o]$, demonstrates a dependence on the load resistance estimation variance. Hence,

$$\delta R_L = R_L\prime - R_L \tag{24}$$

$$\delta V_o = V_o\prime - V_o \tag{25}$$

are the resulting error terms of the estimated parameters.

Utilizing the system specifications provided in Table 1, load resistance and output load voltage are estimated analytically. Figure 4 (a) and (b) provides a quantitative demonstration of Eqs. (21) and (23), respectively, plotting the increasing primary-side current noise variance of 0.1 to 2.5 against the variance of the estimated load resistance R_L and output voltage V_o. In Fig. 4 (a), the variance of the estimated R_L rises from less than 0.01 Ω^2 to approximately 0.24 Ω^2 while Fig. 4 (b) shows that the variance of V_o increases from less than 0.01 Ω^2 to approximately 0.12 V_o^2. The accelerating growth in the variance of both estimates confirms that the sole analytical method inherently amplifies measurement uncertainty, leading to unreliable and imprecise results as noise increases. Figure 5 demonstrates the consequence of this unreliability by plotting the percentage of the resulting error terms in (24) and (25). It illustrates that the increased variance translates into reduced estimation accuracy for both the estimated R_L and the subsequent V_o estimation.

Figure 6 (a) demonstrates the R_L estimation while (b) shows the V_o estimation. It can be seen that the identification following a step change exhibits increased deviation error from the actual value, that is propagated in V_o which follows R_L estimation. Estimation error for R_L estimation is 0.5% and 7.1% before and after load step change, respectively, while in V_o estimation error is 2.4% and 7.9% before and after the load step change, respectively. Also, the signal noise is considered in the current measurement. This affects the prior R_L identification and is amplified in subsequent V_o estimation. The estimated load parameters are erroneous in terms of reduced accuracy and sensitivity to noise.

As can be seen, conventional analytical identification method of the IWPT of the system without any update

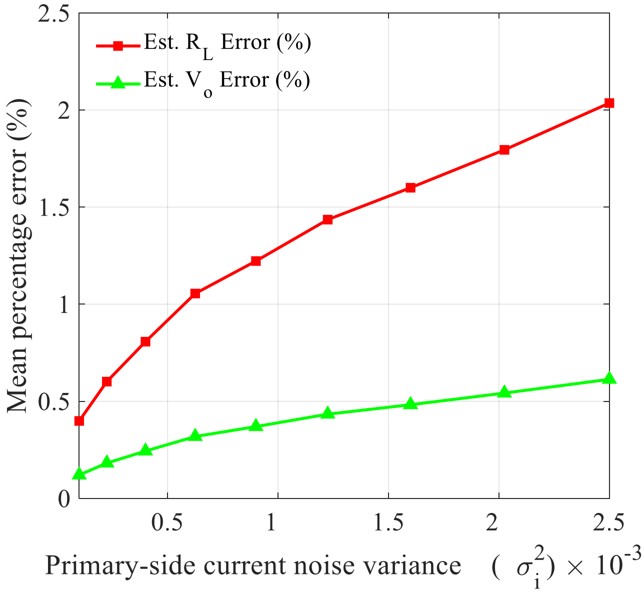

Fig. 5 Comparison of mean percentage error of estimated R_L and V_o

has major drawbacks. First, sole analytical method lacks dynamic adaptability to system changes. If variation in the load occurs during system operation, a fixed analytical solution is not able to adjust flexibly and accordingly. Second, analytical models are susceptible and vulnerable to noise. Since the model assumes a noiseless system, any measurement noise from the sensor or uncertainty noise in the practical system can lead to amplification of error during identification. When sensed values are used in the model, noise in the sensed quantities will propagate through the analytical formula to the identified output parameters, being amplified in the process.

In summary, a sole analytical approach is vulnerable as it is not as accurate outside the idealized set of nominal operation. By contrast, an identification method that is insusceptible to noise would robustly enhance parameter estimation.

3 Proposed Two-Step Identification Method

The two-step identification strategy of an SS-compensated IWPT system proposed in this paper is illustrated in Fig. 7. The first step of this strategy is the identified equivalent load resistance R_{eq} parameter. This quantity has been analytically recognized in the procedure provided in Sect. 2.

Having successfully acquired this baseline parameter, a Kalman estimator is modelled for the output load voltage V_o identification in the second step. To implement the Kalman

Fig. 6 Analytical-based conventional estimation of (**a**) load resistance and (**b**) load voltage

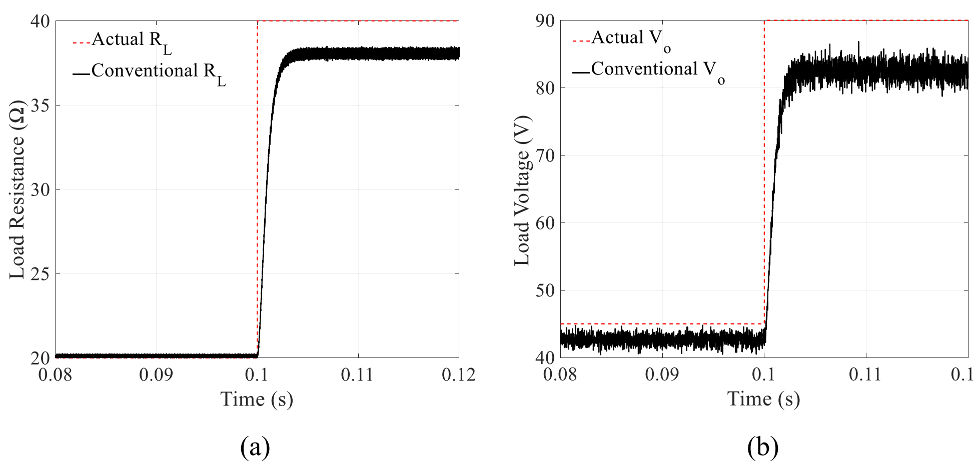

Fig. 7 Two-step identification of an SS-compensated IWPT system

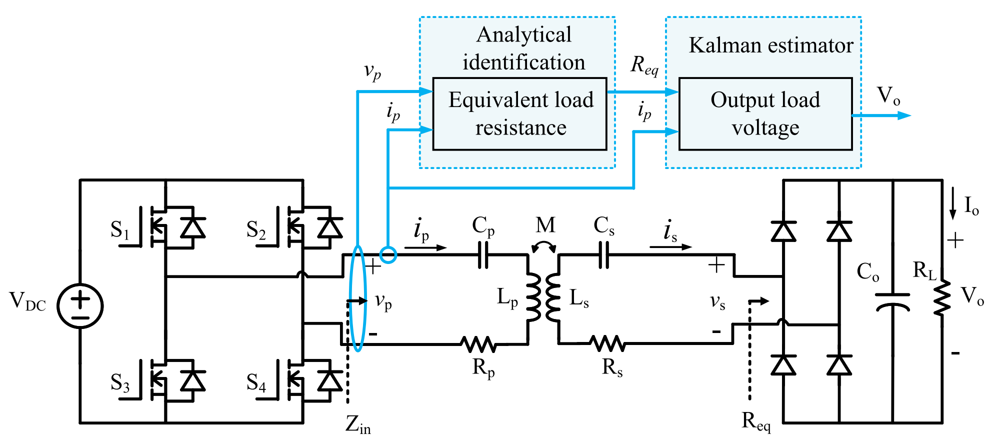

estimator, a state-space representation of the system is first established. The state variables are defined as

$$\boldsymbol{X} = [x_1, x_2, x_3, x_4]^T = \left[i_p, i_s, v_{C_p}, v_{C_s}\right]^T, \tag{26}$$

to describe the state in the energy storage elements in the context of the equivalent circuit of this IWPT system. From Fig. 8 which illustrates a magnetically coupled IWPT system with mutual inductance modelled as current-controlled voltage sources, state equations are obtained as shown in

$$M\dot{x_1} = R_{eq}x_2 + L_s\dot{x_2} + R_s x_2 + x_4, \tag{27}$$

$$u = x_3 + R_p x_1 + L_p\dot{x_1} + M\dot{x_2}, \tag{28}$$

$$\dot{x_3} = \frac{1}{C_p}x_1, \tag{29}$$

$$\dot{x_4} = \frac{1}{C_s}x_2. \tag{30}$$

Solving the state-space equations results in state transition matrix A, input matrix B, output matrix C and direct transition matrix D, that model the dynamic behaviour of the IWPT system. These matrices are

$$A = \begin{bmatrix} \frac{-R_p L_s}{L_i} & \frac{M(R_s+R_{eq})}{L_i} & \frac{-L_s}{L_i} & \frac{M}{L_i} \\ \frac{R_p M}{L_i} & \frac{-L_p(R_s+R_{eq})}{L_i} & \frac{M}{L_i} & \frac{-L_p}{L_i} \\ \frac{1}{C_p} & 0 & 0 & 0 \\ 0 & \frac{1}{C_s} & 0 & 0 \end{bmatrix} \tag{31}$$

$$B = \begin{bmatrix} \frac{L_s}{L_i} & \frac{-M}{L_i} & 0 & 0 \end{bmatrix}^T \tag{32}$$

$$C = [1 \quad 0 \quad 0 \quad 0] \tag{33}$$

$$D = [0] \tag{34}$$

where $L_i = L_p L_s - M^2$ assumes imperfect coupling and k here refers to the iteration index. The Kalman estimator is now utilized to discretely(subscript $_d$) model

$$\boldsymbol{x}(k) = A_d\boldsymbol{x}(k-1) + B_d\boldsymbol{u}(k-1) + w(k-1), \tag{35}$$

$$\boldsymbol{z}(k) = C\boldsymbol{x}(k-1) + v(k-1), \tag{36}$$

$$V_o = \frac{2\sqrt{2}}{\pi}R_{eq}\boldsymbol{z}(k), \tag{37}$$

where $\boldsymbol{x}(k)$ is the four-by-one state vector of the parameter to be estimated which in this case is $\boldsymbol{x}(k)$=[x_1 x_2 x_3 x_4]^T, $\boldsymbol{z}(k)$ is the one-by-one observation vector that corresponds to matrix C of the true state of $\boldsymbol{x}(k)$, $w(k)$ is the process noise and $v(k)$ is the measurement noise. Since i_s is obtained from the result of $\boldsymbol{z}(k)$ and R_{eq} has already been identified, the output DC voltage V_o is achieved after the bridge rectification in (37). The Kalman estimator operates in two phases of prediction and correction [17] as follows:

1) prediction (time update)

$$\hat{\boldsymbol{x}}(k|k-1) = A_d\hat{\boldsymbol{x}}(k-1|k-1) + B_d\boldsymbol{u}(k-1) + w(k-1) \tag{38}$$

$$\boldsymbol{P}(k|k-1) = A_d\boldsymbol{P}(k-1|k-1)A_d^T + Q(k) \tag{39}$$

2) correction (measurement update)

$$\boldsymbol{K}(k) = \boldsymbol{P}(k|k-1)C^T\left(C\boldsymbol{P}(k|k-1)C^T + R(k)\right)^{-1} \tag{40}$$

$$\hat{\boldsymbol{x}}(k|k) = \hat{\boldsymbol{x}}(k|k-1) + \boldsymbol{K}(k)\left(\boldsymbol{z}(k) - C\hat{\boldsymbol{x}}(k|k-1)\right) \tag{41}$$

$$\boldsymbol{P}(k|k) = \left(I - \boldsymbol{K}(k)C\right)\boldsymbol{P}(k|k-1) \tag{42}$$

In this Kalman operation, $\boldsymbol{P}(k)$ is the covariance matrix that measures the estimated accuracy of the state estimate and $\boldsymbol{K}(k)$ is the Kalman gain that optimally balances the trust between the prediction of the system model and the incoming sensor measurement. Here, a high gain places more trust in the measurement while a low gain favors the prediction.

$Q(k)$ and $R(k)$ are noise covariance matrices from the uncertainty of the dynamic system model and measurements obtained through sensors, respectively. Tuning of these covariance parameters aids in achieving stable filter performance. In theory, these matrices should match the true noise statistics, but in most practical applications the exact distributions of process and measurement noise are unknown, hence $Q(k)$ and $R(k)$ effectively become tuning parameters [20]. Following this, the basis for selecting and tuning the parameters of matrices of the noise covariance matrices $Q(k)$ and $R(k)$ is via heuristic trial and error for the filter performance.

Computational speed is also of importance when it comes to real-time implementation of an identification technique. Regarding the case of load variation in the dynamic IWPT system, the time for executing the identification algorithm

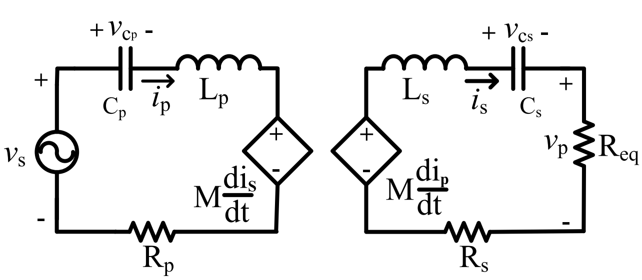

Fig. 8 Schematic of a magnetically coupled IWPT system

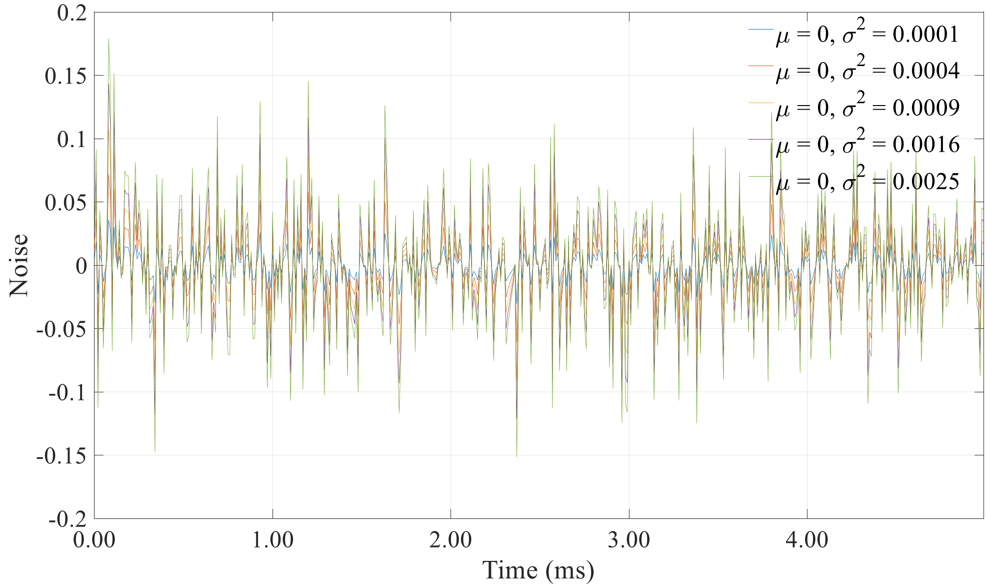

Fig. 9 Additive white gaussian noise injected into the sensed current

will depend on the complexity of the estimation process. The estimator depends on the number of floating point operations required and the number of tasks a processor can handle within a specified period. Calculation of the computation time is done by taking the product of the floating point operations performed per second and the clock speed which is 200 MHz for TMS320F28379D [21]. For the proposed two-step identification, approximately 481 arithmetic operations for equations (31)-(37) are executed. Therefore, assuming 200 million floating point operations per second the estimation computation time is 481x(1/200000000)≈0.002405 s. For the sole analytical-based conventional identification comprising of approximately 167 arithmetic operations performed for equations (6), (10), the computation time for the estimation is 167x(1/200000000)≈0.000835 s. The proposed identification approach computation time is noted to be longer compared to the conventional method due to composition of state-space matrices.

In summary, the proposed two-step identification method strategically decouples the nonlinear system to be estimated. The primary goal of the first step is state-space linearization by analytically providing an estimate for R_{eq} which becomes a known varying parameter of state-space matrix A. Subsequently, second step employs a linear Kalman estimator whose superior ability is to minimize measurement noise and track dynamic changes.

4 Verification

4.1 Simulation Verification

Simulation of a SS-compensated IWPT system is conducted in PSIM software [22] to verify the two-step identification

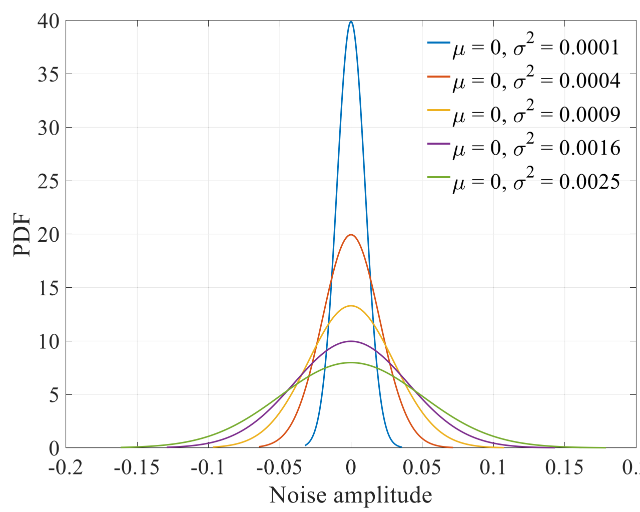

Fig. 10 Probability distribution of noise amplitude

approach utilizing the specification parameters in Table 1. Also, to account for noise in the simulation, Fig. 9 shows AWGN that is injected into the simulation to imitate a practical current sensor that has inherent measurement noise. In the probability distribution plot of the injected noise amplitudes, shown in Fig. 10 of the probability density function (PDF), sigma (σ) is set between 0.01 and 0.05, corresponding to nominal noise levels of 1% to 5% of the measured value. Interpreted statistically, approximately 68% of the noisy measurements do lie within $\pm\sigma$, and about 95% lie within $\pm 2\sigma$ of the true value. A value of σ=0.05 is chosen to emulate a worst-case scenario, where the sensor exhibits relatively high variability, that is, up to ±5% for one standard deviation in its acquired measurements. Also, the noise covariance parameters of $Q(k)$ and $R(k)$ for tuning the behavior of the filter in this simulation are set as

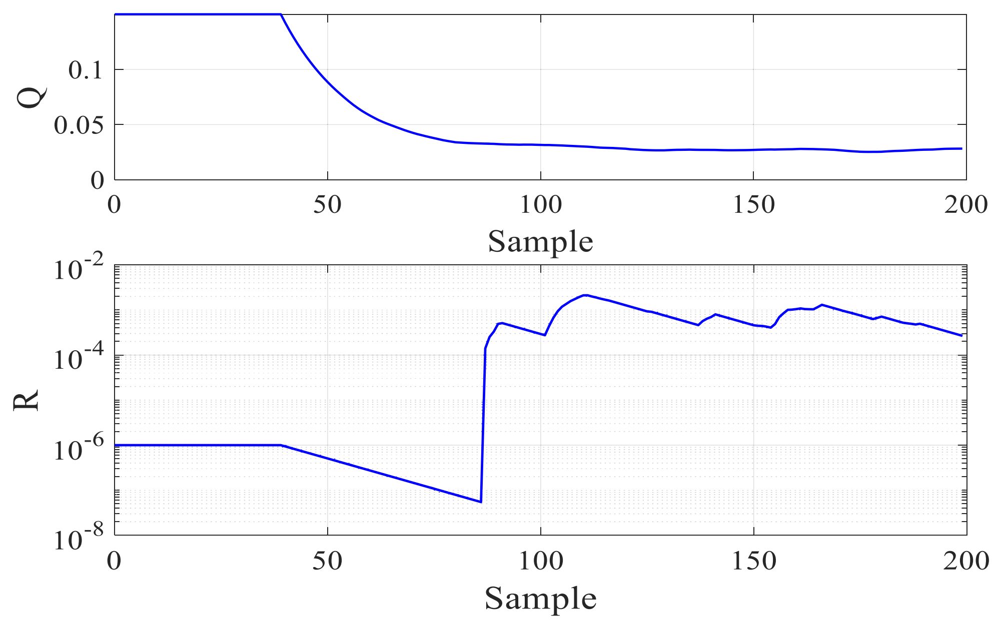

Fig. 11 Tuning noise covariance matrix Q and R parameters

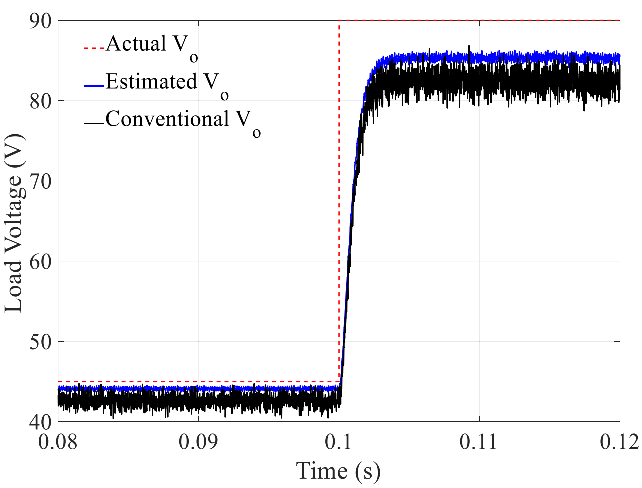

Fig. 12 Simulation result with load step change for output voltage estimation

$$Q(k) = \begin{bmatrix} 0.03 & 0 & 0 & 0 \\ 0 & 0.03 & 0 & 0 \\ 0 & 0 & 0.03 & 0 \\ 0 & 0 & 0 & 0.03 \end{bmatrix} \quad (43)$$

$$R(k) = 10^{-8}. \quad (44)$$

As demonstrated in [23], noise covariances $Q(k) = K(k)I(k)K(k)^T$ and $R(k) = I(k) - CP(k)C^T$ are initialized and adjusted. In the Kalman filter for this system, these covariance matrices are initialized and iteratively tuned as shown in the illustration in Fig. 11 of arbitrary 200 samples under the following selection basis:

(a) Initialize noise covariance parameter values.
(b) Observe for difference between predicted and measured value.
(c) Heuristic tuning of $Q(k)$ and $R(k)$ matrix values.

The selected values from the tuning are then utilized as the respective $Q(k)$ and $R(k)$ covariance matrices parameter values in the system simulation.

Figure 12 illustrates the estimated output voltage when a disturbance is introduced in the load resistance parameter to observe the performance of the two-step identification. From the simulation plot, the two-step identification with Kalman estimator achieves steady-state errors of 1.8% and 4.6% before and after the load step change, respectively, while a 7.9% error deviation is observed for the conventional analytical identification. The Kalman estimator is observed to be robust to sensed noise as well as propagated noise in the output voltage estimation. Hence, the limitation of sole analytical approach method to system dynamic change is observed.

Overall, the proposed two-step estimation approach improves performance for load parameter identification in dynamic conditions since the Kalman estimator adaptively filters noise and tracks dynamic changes with minimized error.

4.2 Experimental Verification

An experimental hardware testing platform for a 75 W IWPT with 50 V input and 40 V output is set up as shown in Fig. 13 to evaluate the proposed identification method using the specifications provided in Table 1. The primary-side power source (ITECH IT-M3413) is bidirectional DC power supply. This supply feeds a full-bridge inverter stage that utilizes high-performance power MOSFETs (CREE C3M0065100k, Silicon Carbide (SiC)) that are suitable for

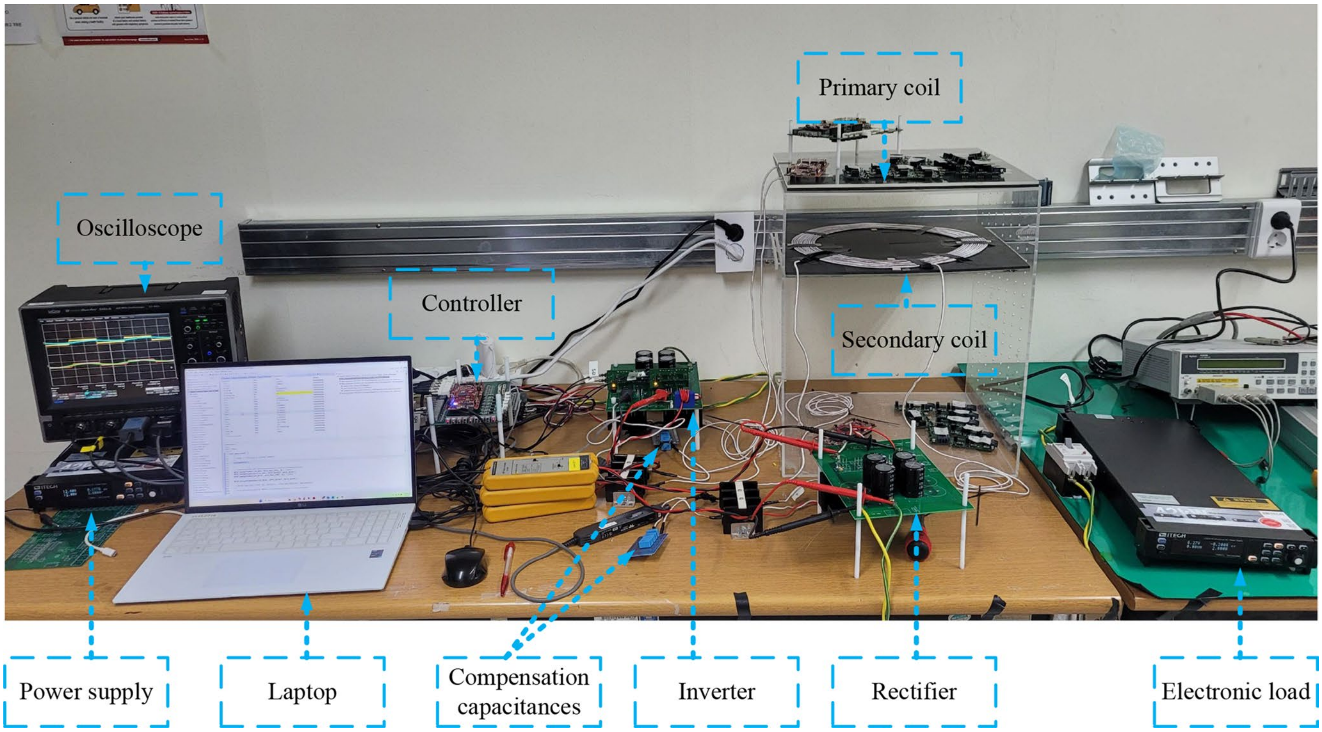

Fig. 13 Experimental hardware setup

high-frequency applications. The transmitter and receiver coils are constructed using 3.5 mm diameter Litz wire to mitigate skin and proximity effects at high frequencies. The primary coil has an inner radius of 130.7 mm and an outer radius of 175.8 mm, while the secondary coil has an inner radius of 126.9 mm and an outer radius of 171.0 mm. For this study, the coils were maintained at a separation distance of 130.4 mm which provides a mutual inductance value of 41.54 μH. Compensation circuit component's measurements are obtained using LCR Meter (Agilent 4263B). These loop coils are mounted on 40 mm by 40 mm ferrite square plates on both sides to provide magnetic flux shaping and shielding.

On the secondary-side, a full-wave rectifier is implemented using Schottky diodes (CREE C3D16060, SiC) and a DC electronic load serves as a variable load for this testing purpose. The system is operated with a 50 V input voltage and an output voltage of 40 V. A current sensor (LEM LA 55-P) is used to obtain current readings of the primary-side current which is then passed through a peak detector. Differential probes (SI-9002) and current probes (LeCroy CP030) are used to measure voltage and current waveforms, respectively, onto the oscilloscope (LeCroy WaveSurfer 64Xs-A). The parameter identification is implemented by utilizing a microcontroller unit (MCU) (Texas Instruments TMS320F28379D) [21]. Sensed current signal is fed into the MCU via configured 12-bit analog-to-digital conversion (ADC). The identified parameters are then converted to analog output signals of the MCU using 12-bit digital-to-analog converter (DAC) whose output conversion value of V_{DAC} is [24]

$$V_{DAC} = V_{ref}\frac{D}{2^n} \tag{45}$$

where V_{ref} is the reference voltage which in this setup is 5 V, D is the digital code decimal value, n is the number of bits (resolution) used to quantify the output and 2^n is the total combination which for 12-bit resolution is 4096.

Figure 14 displays the experimental waveforms of the IWPT system operating at a switching frequency of 114 kHz. The i_p slightly lags v_p, which indicates the desired inductive input impedance for achieving Zero Voltage Switching (ZVS) and minimizing inverter switching losses. On the secondary side, the voltage vs and current i_s are in phase, signifying that the secondary presents a purely resistive load, ensuring efficient real power delivery. These waveforms provide clear validation of the theoretical system model.

Load resistance identification obtained analytically under dynamic system operation with varying load resistance is shown Fig. 15. For observability within the DAC range [24], the output is transformed by 10:1 ratio. As the load resistance is gradually increased, dynamic estimation of R_L is also observed in real time. R_L is varied from 20 Ω to 40 Ω. At nominal 20 Ω, the estimated R_L has about 2% error, and at 40 Ω, the estimation error increases to approximately

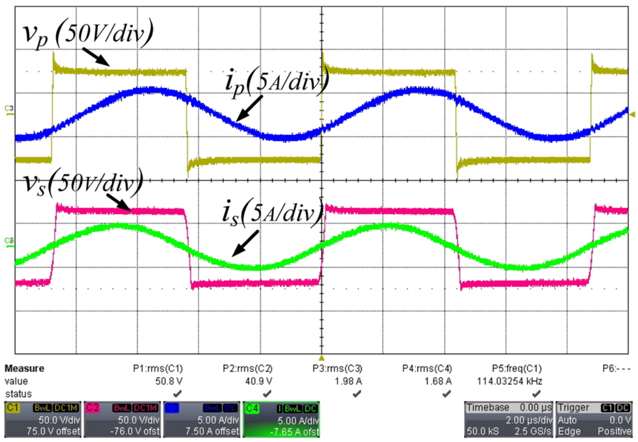

Fig. 14 Experimental waveform of the SS-compensated IWPT

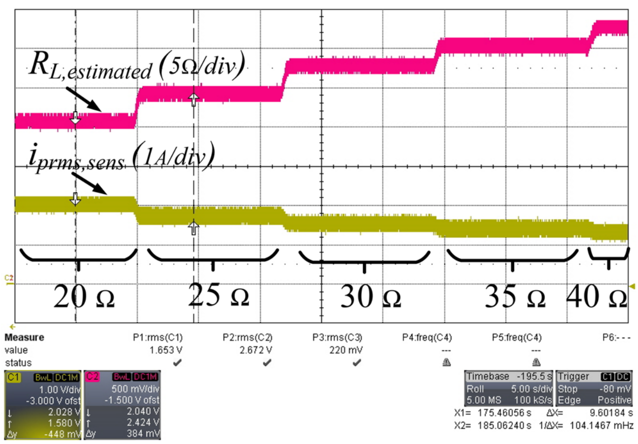

Fig. 15 Load resistance estimation

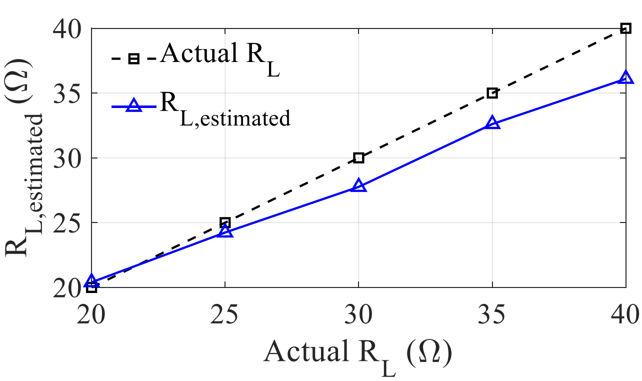

Fig. 16 Comparison of estimated load resistance

9%. It can also be seen that with increasing load resistance, the primary-side rms current decreases gradually as well, which decreases the current sensing accuracy thus affecting the estimation of R_L. As such, the best identification with least errors occurs when R_L is observed to be between 20 Ω and 25 Ω. Figure 16 demonstrates the deviation trend of the estimated load resistance. Similar to the simulated outcome of the estimated load resistance, the $R_{L,estimate}$ is able to follow the actual load resistance value with about 9% deviation at the maximum load resistance variation range of 40 Ω.

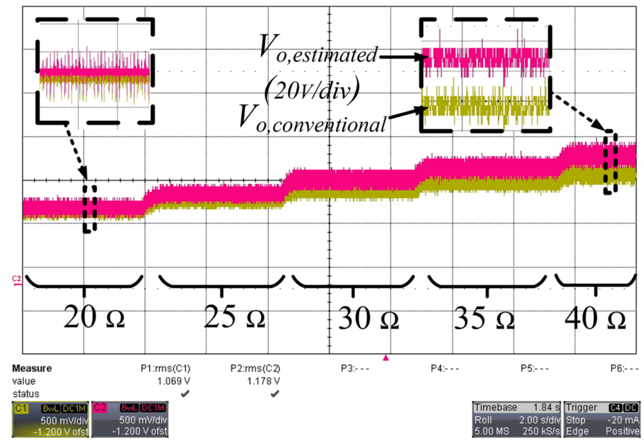

Fig. 17 Output load voltage estimation comparison

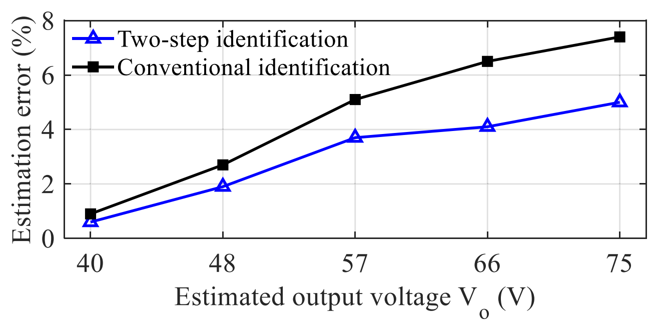

Fig. 18 Voltage estimation error comparison

Figure 17 shows the comparison of the estimated output load voltage V_o between the conventional sole analytical method and the proposed two-step identification method. The output voltage is plotted after computation via DAC [24]. For observability within the DAC range, the output is transformed by 40:1 ratio. At nominal voltage of 40 V the estimation is seen to have small errors in both estimation approaches. The estimation of the two-step Kalman estimator has approximately 5% error while conventional estimation has approximately 7.4% error at maximum load change. This is because with increasingly varying load resistance, the error in the prior estimated parameter of $R_{L,estimated}$ increases as well, impacting output voltage estimation. This increase is illustrated with the increasingly varying load resistance in both methods in Fig. 18. However, the conventional method is increasingly more erroneous as it is noisy. Compared to conventional estimation the proposed identification approach mitigates the noise as it reduces the error by approximately 32% at maximum load resistance variation. Hence, the two-step identification proves to mitigate the noise as load continuously varies. The performance obtained in this work is comparable with various reported

Table 2 Performance comparison of primary-side identification methods

Ref.	Online Identification	Additional Hardware	Maximum Estimation Error	Computation Speed	System Complexity
[7]	X	O	<6.6%	Not mentioned	Medium
[15]	X	O	<1.7%	Within 8 ms	High
[12]	O	X	<7.4%	2s	Low
[10]	O	X	<7%	Not mentioned	Medium
[25]	O	X	<2%	Within 10 ms	High
This work	O	X	≤5%	Within 3 ms	Low

identification techniques of IWPT systems in literature as shown in Table 2. The performance comparison among the conventionally proposed primary-side identification techniques considers several trade-offs in the implementation process as reported in their respective works.

5 Conclusion

In this article, a two-step identification strategy combining analytical modeling with a state-space Kalman estimator has been presented to estimate output parameters in communication-less dynamic IWPT systems. By first deriving a baseline equivalent load resistance analytically and then applying a linear Kalman estimator to track the output load voltage, the method suppresses noise propagation and adapts to load variations without disrupting system operation. It demonstrates significantly reduced estimation errors under noisy conditions and load changes. The non-disruptive merit of this approach and its primary-side-only implementation make it effective for real-time application in dynamic charging IWPT systems.

Acknowledgements This work was supported by the "Regional Innovation System & Education (RISE)" through the Ulsan RISE Center, funded by the Ministry of Education (MOE) and the Ulsan Metropolitan City, Republic of Korea (2025-RISE-07–001).

Author Contributions Sung-Jin Choi proposed the basic concept of this paper, and Andrew Ngini Mwangi contributed to the mathematical formulation, simulation, hardware implementation and wrote the original manuscript.

Data Availability The contributions and findings presented in this study are included in the article, further inquiries can be directed to the corresponding author.

Declarations

Conflicts of Interest The authors declare that they have no conflict of interest.

References

1. Zhang Z, Pang H, Georgiadis A, Cecati C (2019) Wireless power transfer–an overview. IEEE Trans Ind Electron 66(2):1044–1058. https://doi.org/10.1109/TIE.2018.2835378
2. Xia N, Yan S, Li F, Ma H, Chen M, Mao X (2025) High misalignment-tolerant wireless charging magnetic coupling system with combined pickups for UAVs. J Power Electron 25(4):745–755. https://doi.org/10.1007/s43236-024-00921-2
3. Lu C, Ni Y, Song K et al (2025) Analysis and design of U-shaped wireless power transfer system for humanoid robots. J Power Electron 25:724–734. https://doi.org/10.1007/s43236-024-00941-y
4. Mahesh A, Chokkalingam B, Mihet-Popa L (2021) Inductive wireless power transfer charging for electric vehicles–a review. IEEE Access 9:137667–137713. https://doi.org/10.1109/ACCESS.2021.3116663
5. Qiang H, Wang J, Xu T (2024) Dual receiver topology for bipolar dynamic wireless power transfer systems. J Power Electron 24:672–682. https://doi.org/10.1007/s43236-023-00424-0
6. Madawala UK, Thrimawithana DJ (2012) New technique for inductive power transfer using a single controller. IET Power Electron 5(2):248–256. https://doi.org/10.1049/iet-pel.2011.0166
7. Guo Y, Zhang Y (2022) Secondary side voltage and current estimation of wireless power transfer systems. IEEE Trans Ind Appl 58(1):1222–1230. https://doi.org/10.1109/TIA.2021.3094476
8. Ngini MA, Truong C-T, Choi S-J (2025) Parameter identification for primary-side control of inductive wireless power transfer systems: a review. IEEE Access 13:15885–15904. https://doi.org/10.1109/ACCESS.2025.10849549
9. Meng X, Qiu D, Lin M, Tang SC, Zhang B (2018) Output voltage identification based on transmitting side information for implantable wireless power transfer system. IEEE Access 7:2938–2946. https://doi.org/10.1109/ACCESS.2018.2886856
10. Zeng J, Wu J, Li K, Yang Y, Hui SYR (2024) Dynamic monitoring of battery variables and mutual inductance for primary-side control of a wireless charging system. IEEE Trans Ind Electron 71(7):7966–7974. https://doi.org/10.1109/TIE.2023.3315690
11. Liao Z-J, Gao B, Yi F, Liu Z-P, Jin Z-Y, Xia C-Y (2024) A universal mutual inductance and load identification methodology for MC-WPT systems with arbitrary topology. IEEE Trans Power Electron 39(12):16943–16954. https://doi.org/10.1109/TPEL.2024.10660563
12. Dai R, Zhou W, Chen Y, Zhu Z, Mai R (2022) Pulse density modulation based mutual inductance and load resistance identification method for wireless power transfer system. IEEE Trans Power Electron 37(8):9933–9943. https://doi.org/10.1109/TPEL.2022.3163011
13. Huang Q, Deng Q, Li Z et al (2024) Application of a modified wavelet threshold denoising algorithm in system identification of WPTS. J Power Electron 24:1150–1162. https://doi.org/10.1007/s43236-024-00788-3
14. Yin J, Lin D, Lee CK, Parisini T, Hui SY (2015) Front-end monitoring of multiple loads in wireless power transfer systems without wireless communication systems. IEEE Trans Power Electron 31(3):2510–2517. https://doi.org/10.1109/TPEL.2015.2439634
15. Zeng J, Yang Y, Li K, Chen S, Hui SYR (2023) An ultrafast estimation method for coupling coefficient and receiver resonant frequency in universal wireless power transfer systems. IEEE Trans

Power Electron 39(4):4870–4883. https://doi.org/10.1109/TPEL.2023.3238927
16. Li Z, Liu H, Tian Y, Liu Y (2021) Constant current/voltage charging for primary-side controlled wireless charging system without using dual-side communication. IEEE Trans Power Electron 36(12):13562–13577. https://doi.org/10.1109/TPEL.2021.3079305
17. Li Q, Li R, Ji K, Dai W (2015) Kalman filter and its application. In 2015 8th International Conference on Intelligent Networks and Intelligent Systems (ICINIS), IEEE (pp. 74–77). https://doi.org/10.1109/ICINIS.2015.23
18. Karami Z, Guidi G, Suul JA (2024) Coupling coefficient and load estimation for model predictive control of inductive power transfer systems with constant voltage load. In Proceedings of the IEEE International Conference on Industrial Technology (ICIT), IEEE (pp. 1–6). https://doi.org/10.1109/ICIT59640.2024.10575649
19. Wireless Power Consortium (WPC) (2018) The Qi wireless power transfer system – power class 0 specification. IEEE Access *1.2.4*(4)
20. Kim Y, Bang H (2018) Introduction to Kalman filter and its applications. IntechOpen 1–16. https://doi.org/10.5772/intechopen.80600
21. Texas Instruments (2024 February) TMS320F2837xD dual-core real-time microcontrollers (TMS320F28379D datasheet). Dallas, TX, USA. Retrieved August 2025, from https://www.ti.com/product/TMS320F28379D
22. Altair (2025) Power electronics and motor drive software – Altair® PSIM™. Retrieved August 2025, from https://altair.com/psim-applications
23. Mehra RK (1970) On the identification of variances and adaptive Kalman filtering. IEEE Trans Autom Control 15(2):175–184. https://doi.org/10.1109/TAC.1970.1099422
24. Texas Instruments (2025) DAC7554IDGS — low-power, low-Glitch, 12-bit DAC (VSSOP-10). Retrieved August 2025, from Dallas, TX, USA. https://www.ti.com/product/DAC7554/part-details/DAC7554IDGS
25. Lee S, Lee S-H (2025) Observer-based online parameter identification of series–series tuned inductive power transfer system. IEEE Trans Ind Electron 72(3):2927–2937. https://doi.org/10.1109/TIE.2024.3423413

Andrew Ngini Mwangi was born in Nairobi, Kenya. He received his B.S. degree in Electronics Engineering from Hanyang University, Seoul, South Korea, in 2022. He is currently working towards the M.S. degree in electrical engineering at the University of Ulsan, Ulsan, South Korea. His research interests include wireless power transfer and power converters.

Sung-Jin Choi received his B.S., M.S., and Ph.D. degrees in Electrical Engineering from Seoul National University, Seoul, South Korea, in 1996, 1998, and 2006, respectively. From 2006 to 2008, he was a Research Engineer with Palabs Company Ltd., Seoul, South Korea. From 2008 to 2011, he was the Principal Research Engineer with Samsung Electronics Company Ltd., Suwon, South Korea, where he was responsible for developing LED drive circuits and wireless battery charging systems. In 2011, he joined the University of Ulsan, Ulsan, South Korea, where he is presently working as Professor in the Department of Electrical, Electronic and Computer Engineering. He was a Visiting Scholar at San Diego State University, San Diego, CA, USA from 2017 to 2018 and at University of Colorado Denver, Denver, CO, USA in 2022. His current research interests include modeling and control of high-frequency power converters in solar power generation, battery management, and wireless power transfer. He is the Editor-in-Chief of the *Journal of Power Electronics*.